Multi-Frequency Deterministic Inversion of Wideband GPR Data: Achievable Performance in the Presence of Unknown Background Media

M. Salucci, L. Poli, and A. Massa

Abstract

This work deals with the retrieval of the electromagnetic properties of buried investigation domains starting from the processing of wideband ground penetrating radar (*GPR*) data. More precisely, the achievable performance by two deterministic multi-zooming (*IMSA*) conjugate gradient (*CG*)-based techniques are assessed when no exact knowledge of the electric permittivity of the background is available to perform the inversion. More precisely, the first analyzed technique is based on a multi-frequency (*MF*) approach (i.e., the *MF-IMSA-CG*), while the second one is a state-of-the-art frequency-hopping (*FH*) based methodology (i.e., the *FH-IMSA-CG*). Some significant numerical results are reported in order to understand what is the impact of a wrong guess of the hosting medium under several noise conditions for both *MF* and *FH*-based inversion methods.

1 Definitions

1.1 Glossary

- D_{inv}: investigation domain;
- D_{obs}: observation domain;
- N: number of discretization cells in D_{ind};
- V: number of views;
- M: number of measurement points;
- F: number of frequencies considered for the inversion;
- (x_v, y_v): coordinates of the v-th source $(v = 1, \ldots, V)$.
- (x_m^v, y_m^v): coordinates of the m-th measurement point for the v-th view v, $(m = 1, \ldots, M)$;
- $\varepsilon_{ra} = \frac{\varepsilon_a}{\varepsilon_0}$: relative electric permittivity for the upper half-space $(y > 0)$;
- σ_a: conductivity for the upper half-space $(y > 0)$;
- $\varepsilon_{rb} = \frac{\varepsilon_b}{\varepsilon_0}$: background relative electric permittivity;
- σ_b: background conductivity;

2 Wrong guess of the background permittivity

2.1 Goal of this section

This analysis is devoted at verifying what are the achievable performances by the $MF-IMSA-CG$ [13] and the $FH-IMSA-CG$ [3] approaches when a wrong guess of the background permittivity is used for the inversion

$$\varepsilon_{rB}^{guess} \neq \varepsilon_{rB}^{actual}$$

The following values of ε_{rB}^{guess} will be considered in the following:

1. $\varepsilon_{rB}^{guess} = \varepsilon_{rB}^{actual} \pm 5\%$
2. $\varepsilon_{rB}^{guess} = \varepsilon_{rB}^{actual} \pm 10\%$
3. $\varepsilon_{rB}^{guess} = \varepsilon_{rB}^{actual} \pm 20\%$

2.2 "$\mathcal{I}$-Shaped" object ($\varepsilon_{r,obj} = 5.5$, $\sigma_{obj} = 10^{-3}$ [S/m])

2.2.1 Parameters

Background

Inhomogeneous and nonmagnetic background composed by two half spaces

- Upper half space ($y > 0$ - air): $\varepsilon_{ra} = 1.0$, $\sigma_a = 0.0$;
- Lower half space ($y < 0$ - soil): $\varepsilon_{rb} = 4.0$, $\sigma_b = 10^{-3}$[S/m];

Investigation domain (D_{inv})

- Side: $L_{D_{inv}} = 0.8$ [m];
- Barycenter: $\left(x_{bar}^{D_{inv}}, y_{bar}^{D_{inv}}\right) = (0.00, -0.4)$ [m];

Time-Domain forward solver ($FDTD$ - $GPRMax2D$)

- Side of the simulated domain: $L = 6$ [m];
- Number of cells: $N^{FDTD} = 750 \times 750 = 5.625 \times 10^5$;
- Side of the $FDTD$ cells $l^{FDTD} = 0.008$ [m];
- Simulation time window: $T^{FDTD} = 20 \times 10^{-9}$ [sec];
- Time step: $\Delta t^{FDTD} = 1.89 \times 10^{-11}$ [sec];
- Number of time samples: $N_t^{FDTD} = 1060$;
- Boundary conditions: perfectly matched layer (PML);
- Source type: Gaussian mono-cycle (first Gaussian pulse derivative, called "Ricker" in $GPRMax2D$)
  - Central frequency: $f_0 = 300$ [MHz];
  - Source amplitude: $A = 1.0$ [A];

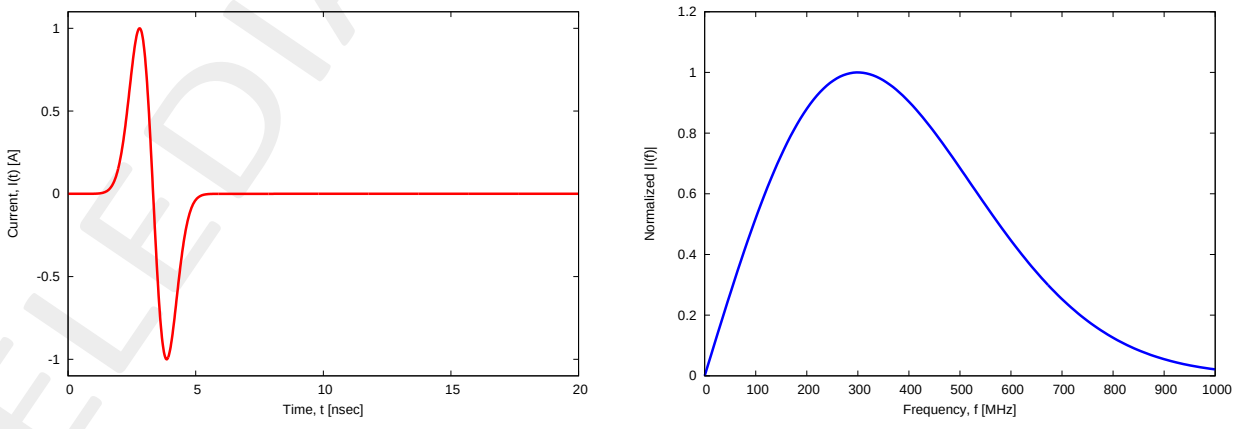

(a) (b)

Figure 1: $GPRMax2D$ excitation signal. (a) Time pulse, (b) normalized frequency spectrum.

Frequency parameters

- Frequency range: $f \in [f_{min}, f_{max}] = [200.0, 600.0]$ [MHz] [?] (-3 [dB] bandwidth of the Gaussian Monocycle excitation centered at $f_0 = 300$ [MHz]);
- Frequency step: $\Delta f = 100$ [MHz] ($F = 5$ frequency steps in $[f_{min}, f_{max}]$);

f [MHz]	λ_a [m]	λ_b [m]	f^* [MHz]
200.0	1.50	0.75	200.5
300.0	1.00	0.50	297.6
400.0	0.75	0.37	401.1
500.0	0.60	0.30	498.1
600.0	0.50	0.25	601.6

Table 1: Considered frequencies and corresponding wavelength in the upper medium (λ_a, free space) and in the lower medium (λ_b, soil). f^* is the nearest frequency sample available from transformed time-domain data, and represents the real frequency considered by the inversion algorithm.

Scatterer

- Electromagnetic properties: $\varepsilon_{r,obj} = 5.5$, $\sigma_{obj} = 10^{-3}$ [S/m] ($\sigma_{obj} = \sigma_b$);
- Contrast function: $\tau = 1.5 + j0.0$

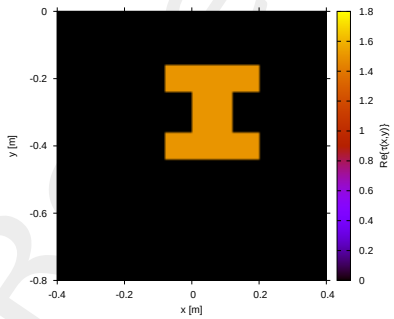

Figure 2: Actual object.

Measurement setup

- Considered frequency: $f_{min} = 200$ [MHz], $\lambda_b = 0.75$ [m].
- $\#DoFs = 2ka = \frac{2\pi}{\lambda_b} L\sqrt{2} = \frac{2\pi}{0.75} 0.8\sqrt{2} \simeq 9.5$;
- Number of views (sources): $V = 10$;
  - $\min\{x_v\} = -0.5$ [m], $\max\{x_v\} = 0.5$ [m];
  - height: $y_v = 0.1$ [m], $\forall v = 1, \ldots, V$;
- Number of measurement points: $M = 9$;
  - $\min\{x_m\} = -0.5$ [m], $\max\{x_m\} = 0.5$ [m];

- height: $y_m = 0.1$ [m], $\forall m = 1, \ldots, M$;

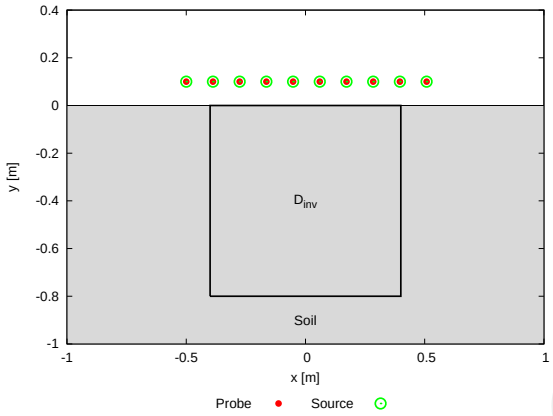

Figure 3: Location of the measurement points ($M = 9$) and of the sources ($V = 10$). Only one source is active for each view.

Inverse solver parameters

- **Shared parameters**
  - Weight of the state term of the functional: 1.0;
  - Weight of the data term of the functional: 1.0;
  - Convergence threshold: 10^{-10};
  - Variable ranges:
    - $\sigma \in \left[8.0 \times 10^{-4}, 1.2 \times 10^{-3}\right]$ [S/m];
    - $\Re\left\{E_{tot}^{int}\right\} \in [-8, 8]$, $\Im\left\{E_{tot}^{int}\right\} \in [-8, 8]$;
  - Degrees of freedom:
    - Considered frequency: $f_{min} = 200$ [MHz], $\lambda_b = 0.75$ [m];
    - $\frac{(2ka)^2}{2} = \frac{\left(2 \times \frac{2\pi}{\lambda_b} \times \frac{L\sqrt{2}}{2}\right)^2}{2} = 4\pi^2 \left(\frac{L}{\lambda_b}\right)^2 = 4\pi^2 \left(\frac{0.8}{0.75}\right)^2 \simeq 44.87$;
  - Number of cells: $N = 49 = 7 \times 7$;
  - Maximum number of $IMSA$ steps: $S = 4$;
  - Side ratio threshold: $\eta_{th} = 0.2$;
- $MF - IMSA - CG$ **parameters**
  - Maximum number of iterations: $I = 200$;
- $FH - IMSA - CG$ **parameters**
  - Maximum number of iterations: $I = 400$;

Signal to noise ratio (on $E_{tot}(t)$)

- $SNR = \{50, 40, 30, 20\}$ [dB] + Noiseless data.

2.2.2 $\varepsilon_{rB}^{guess} = 3.2$: Final reconstructions (@$f_{max} = 600$ [MHz])

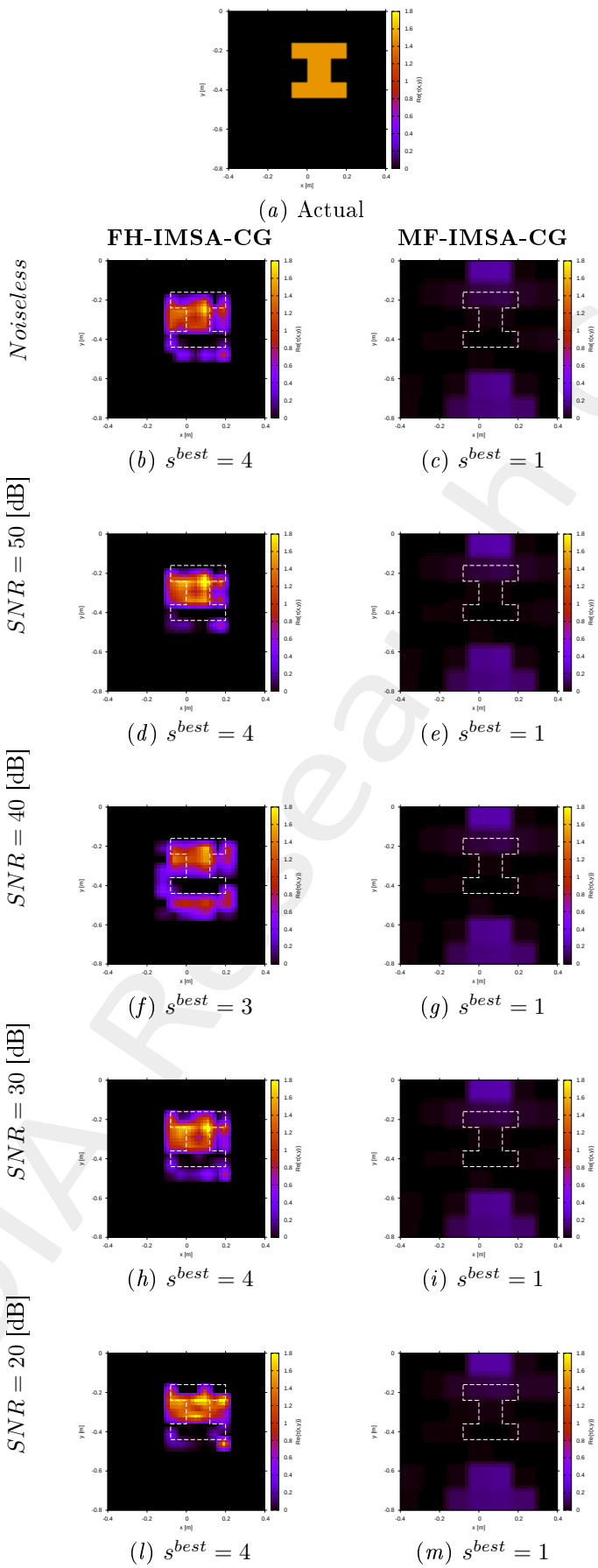

(a) Actual

(b) $s^{best} = 4$ (c) $s^{best} = 1$

(d) $s^{best} = 4$ (e) $s^{best} = 1$

(f) $s^{best} = 3$ (g) $s^{best} = 1$

(h) $s^{best} = 4$ (i) $s^{best} = 1$

(l) $s^{best} = 4$ (m) $s^{best} = 1$

Figure 4: $FH - IMSA - CG$ vs. $MF - IMSA - CG$: Retrieved dielectric profiles at the $IMSA$ convergence step (s^{best}).

2.2.3 $\varepsilon_{rB}^{guess} = 3.6$: Final reconstructions (@$f_{max} = 600$ [MHz])

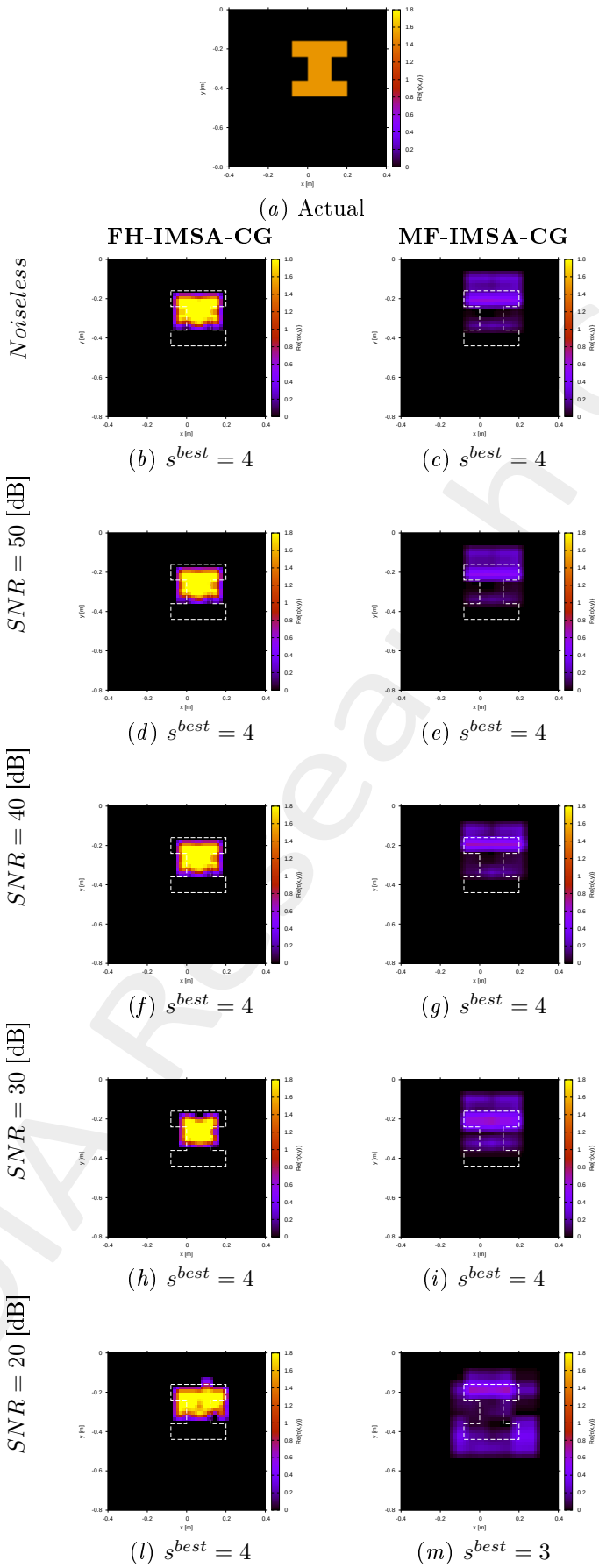

(a) Actual

(b) $s^{best} = 4$ (c) $s^{best} = 4$

(d) $s^{best} = 4$ (e) $s^{best} = 4$

(f) $s^{best} = 4$ (g) $s^{best} = 4$

(h) $s^{best} = 4$ (i) $s^{best} = 4$

(l) $s^{best} = 4$ (m) $s^{best} = 3$

Figure 5: $FH - IMSA - CG$ vs. $MF - IMSA - CG$: Retrieved dielectric profiles at the $IMSA$ convergence step (s^{best}).

2.2.4 $\varepsilon_{rB}^{guess} = 3.8$: Final reconstructions (@$f_{max} = 600$ [MHz])

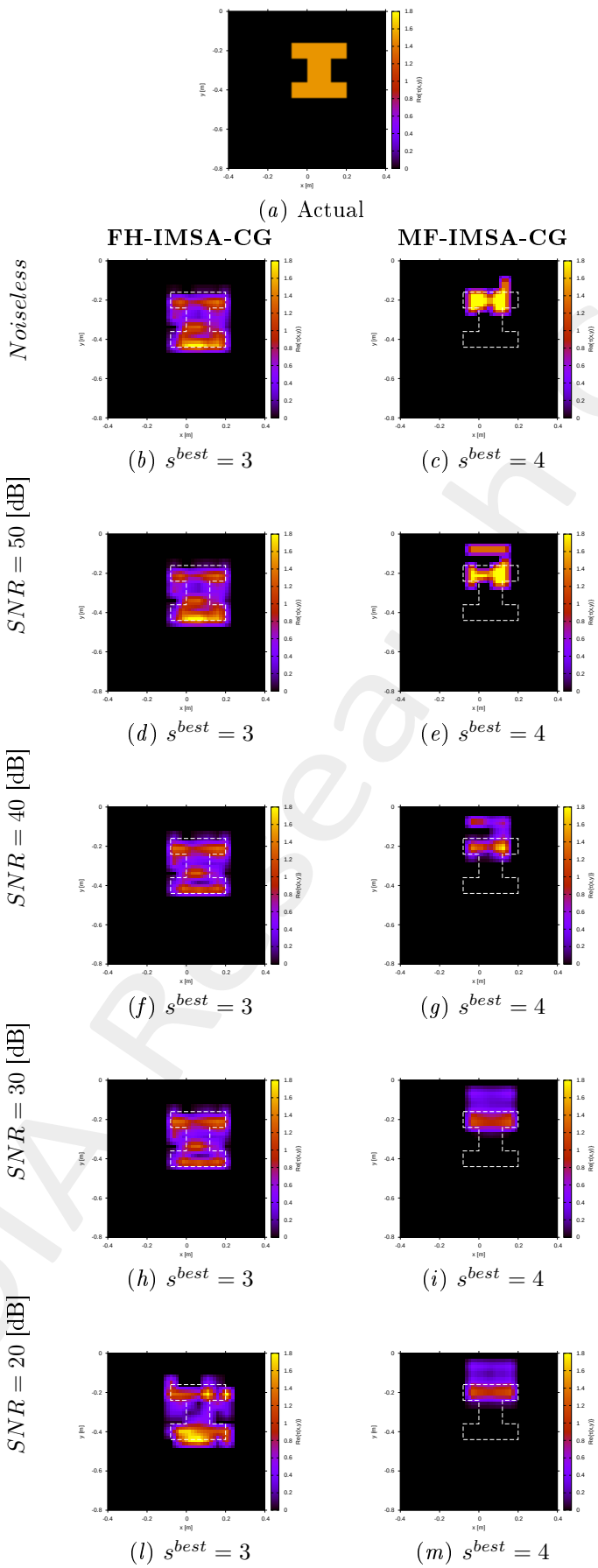

(a) Actual

(b) $s^{best} = 3$ (c) $s^{best} = 4$

(d) $s^{best} = 3$ (e) $s^{best} = 4$

(f) $s^{best} = 3$ (g) $s^{best} = 4$

(h) $s^{best} = 3$ (i) $s^{best} = 4$

(l) $s^{best} = 3$ (m) $s^{best} = 4$

Figure 6: $FH-IMSA-CG$ vs. $MF-IMSA-CG$: Retrieved dielectric profiles at the $IMSA$ convergence step (s^{best}).

2.2.5 $\varepsilon_{rB}^{guess} = 4.2$: Final reconstructions (@$f_{max} = 600$ [MHz])

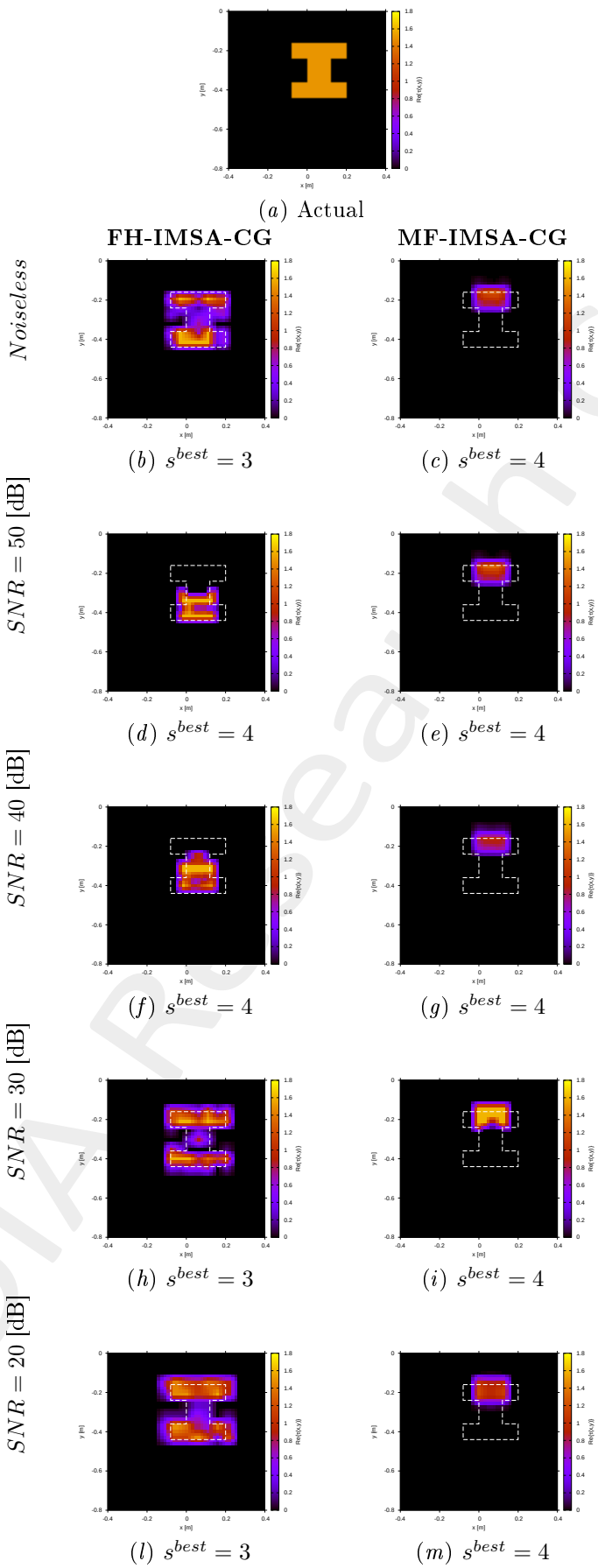

(a) Actual

(b) $s^{best} = 3$ (c) $s^{best} = 4$

(d) $s^{best} = 4$ (e) $s^{best} = 4$

(f) $s^{best} = 4$ (g) $s^{best} = 4$

(h) $s^{best} = 3$ (i) $s^{best} = 4$

(l) $s^{best} = 3$ (m) $s^{best} = 4$

Figure 7: $FH-IMSA-CG$ vs. $MF-IMSA-CG$: Retrieved dielectric profiles at the $IMSA$ convergence step (s^{best}).

2.2.6 $\varepsilon_{rB}^{guess} = 4.4$: Final reconstructions (@$f_{max} = 600$ [MHz])

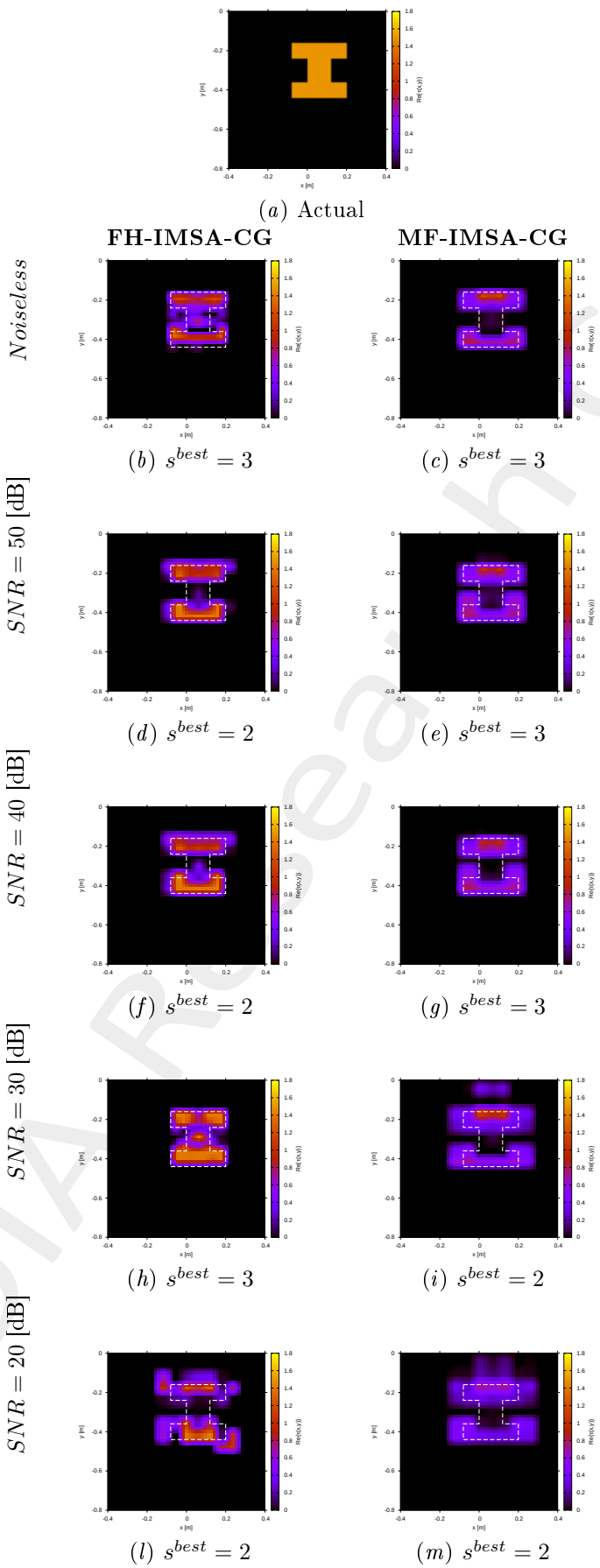

(a) Actual

(b) $s^{best} = 3$ (c) $s^{best} = 3$

(d) $s^{best} = 2$ (e) $s^{best} = 3$

(f) $s^{best} = 2$ (g) $s^{best} = 3$

(h) $s^{best} = 3$ (i) $s^{best} = 2$

(l) $s^{best} = 2$ (m) $s^{best} = 2$

Figure 8: $FH - IMSA - CG$ vs. $MF - IMSA - CG$: Retrieved dielectric profiles at the $IMSA$ convergence step (s^{best}).

2.2.7 $\varepsilon_{rB}^{guess} = 4.8$: Final reconstructions (@$f_{max} = 600$ [MHz])

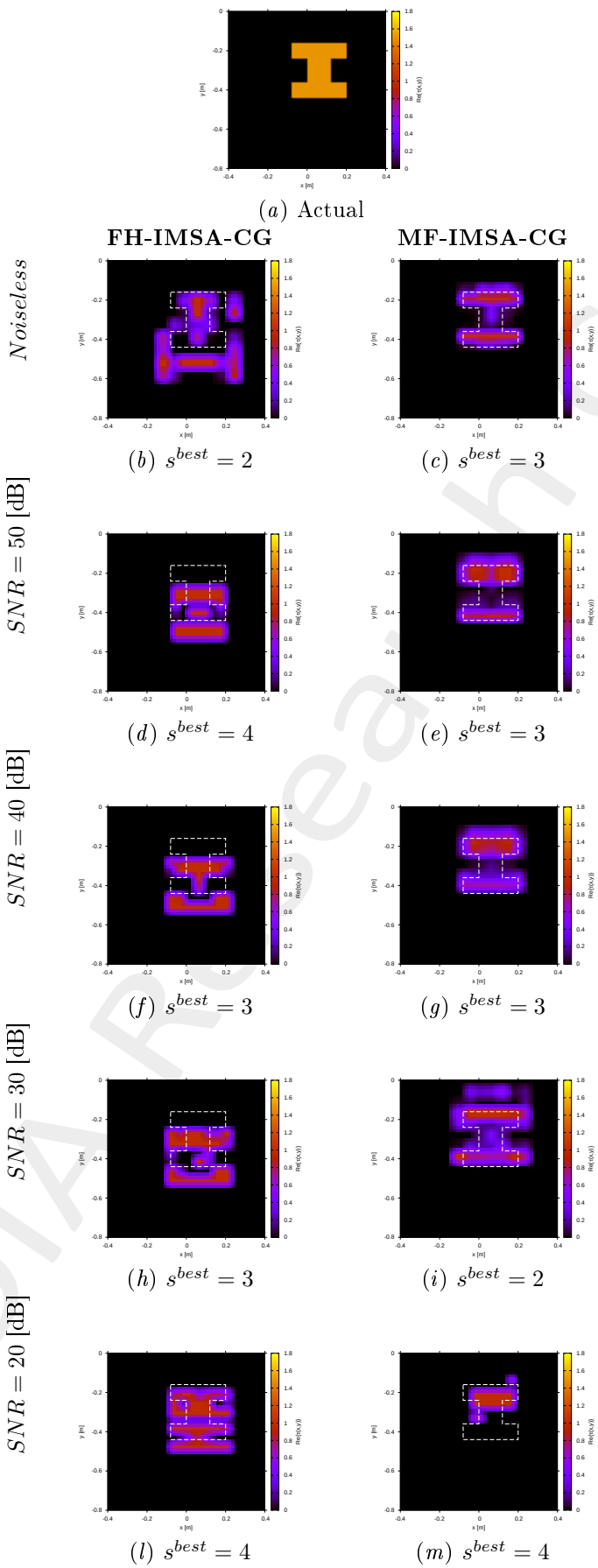

(a) Actual

(b) $s^{best} = 2$ (c) $s^{best} = 3$

(d) $s^{best} = 4$ (e) $s^{best} = 3$

(f) $s^{best} = 3$ (g) $s^{best} = 3$

(h) $s^{best} = 3$ (i) $s^{best} = 2$

(l) $s^{best} = 4$ (m) $s^{best} = 4$

Figure 9: $FH-IMSA-CG$ vs. $MF-IMSA-CG$: Retrieved dielectric profiles at the $IMSA$ convergence step (s^{best}).

2.2.8 Reconstruction Errors vs. ε_{rB}^{guess} (@$f_{max} = 600$ [MHz])

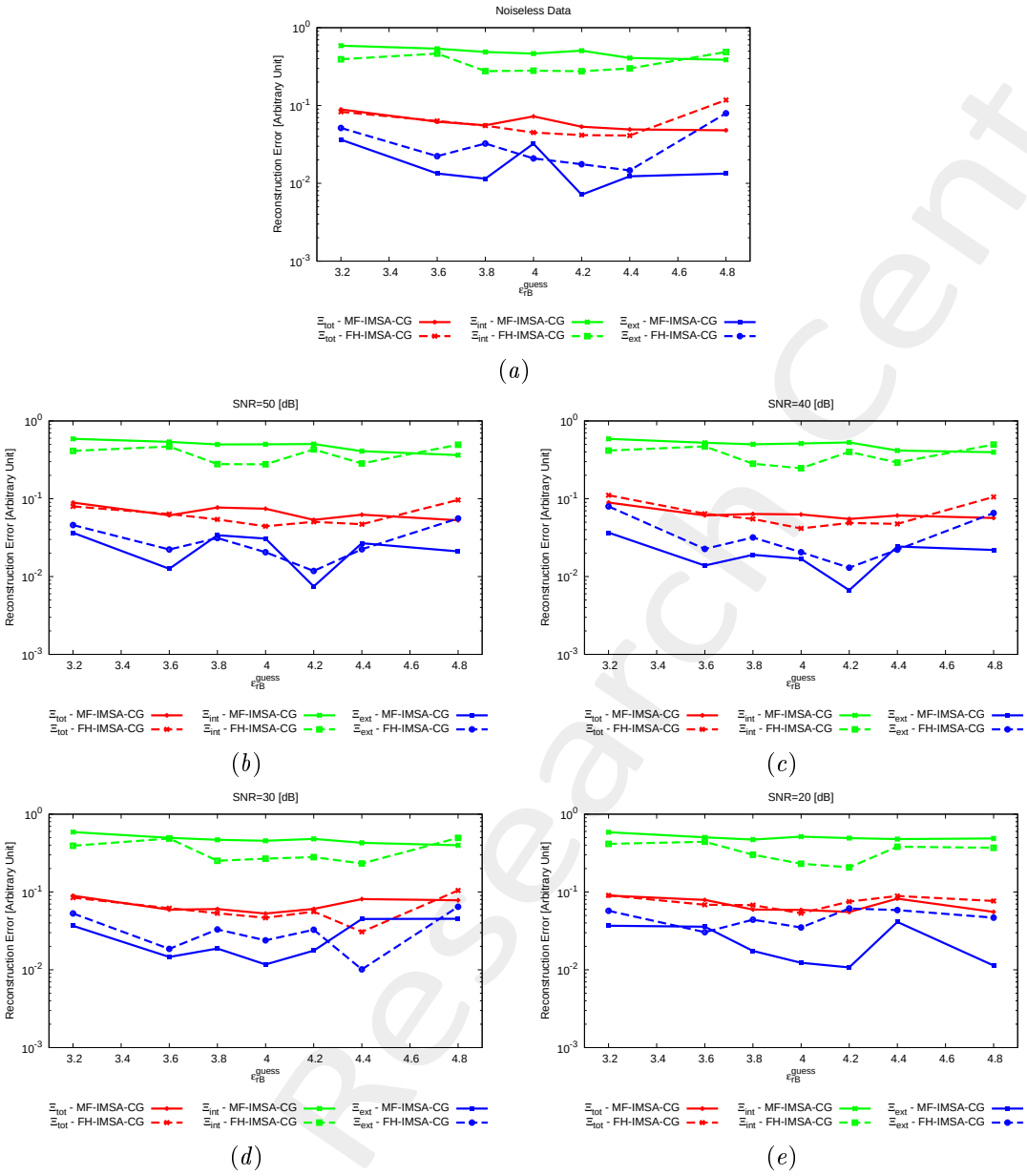

Figure 10: $FH-IMSA-CG$ vs. $MF-IMSA-CG$: Reconstruction errors vs. ε_{rB}^{guess}.

References

[1] P. Rocca, M. Benedetti, M. Donelli, D. Franceschini, and A. Massa, "Evolutionary optimization as applied to inverse problems," *Inverse Probl.*, vol. 25, pp. 1-41, Dec. 2009.

[2] P. Rocca, G. Oliveri, and A. Massa, "Differential Evolution as applied to electromagnetics," *IEEE Antennas Propag. Mag.*, vol. 53, no. 1, pp. 38-49, Feb. 2011.

[3] M. Salucci, G. Oliveri, and A. Massa, "GPR prospecting through an inverse scattering frequency-hopping multi-focusing approach," *IEEE Trans. Geosci. Remote Sens.*, vol. 53, no. 12, pp. 6573-6592, Dec. 2015.

[4] M. Salucci, L. Poli, N. Anselmi and A. Massa, "Multifrequency particle swarm optimization for enhanced multiresolution GPR microwave imaging," *IEEE Trans. Geosci. Remote Sens.*, vol. 55, no. 3, pp. 1305-1317, Mar. 2017.

[5] A. Massa, P. Rocca, and G. Oliveri, "Compressive sensing in electromagnetics - A review," *IEEE Antennas Propag. Mag.*, pp. 224-238, vol. 57, no. 1, Feb. 2015.

[6] A. Massa and F. Texeira, Guest-Editorial: Special Cluster on Compressive Sensing as Applied to Electromagnetics, *IEEE Antennas Wireless Propag. Lett.*, vol. 14, pp. 1022-1026, 2015.

[7] N. Anselmi, G. Oliveri, M. Salucci, and A. Massa, "Wavelet-based compressive imaging of sparse targets," *IEEE Trans. Antennas Propag.*, vol. 63, no. 11, pp. 4889-4900, Nov. 2015.

[8] G. Oliveri, N. Anselmi, and A. Massa, "Compressive sensing imaging of non-sparse 2D scatterers by a total-variation approach within the Born approximation," *IEEE Trans. Antennas Propag.*, vol. 62, no. 10, pp. 5157-5170, Oct. 2014.

[9] T. Moriyama, G. Oliveri, M. Salucci, and T. Takenaka, "A multi-scaling forward-backward time-stepping method for microwave imaging," *IEICE Electron. Expr.*, vol. 11, no. 16, pp. 1-12, Aug. 2014.

[10] T. Moriyama, M. Salucci, M. Tanaka, and T. Takenaka, "Image reconstruction from total electric field data with no information on the incident field," *J. Electromagnet. Wave.*, vol. 30, no. 9, pp. 1162-1170, 2016.

[11] F. Viani, L. Poli, G. Oliveri, F. Robol, and A. Massa, "Sparse scatterers imaging through approximated multi-task compressive sensing strategies," *Microw. Opt. Technol. Lett.*, vol. 55, no. 7, pp. 1553-1557, Jul. 2013.

[12] M. Salucci, L. Poli, and A. Massa, "Advanced multi-frequency GPR data processing for non-linear deterministic imaging," *Signal Processing - Special Issue on 'Advanced Ground-Penetrating Radar Signal-Processing Techniques,'* vol. 132, pp. 306-318, Mar. 2017.

[13] M. Salucci, N. Anselmi, G. Oliveri, P. Calmon, R. Miorelli, C. Reboud, and A. Massa, "Real-time NDT-NDE through an innovative adaptive partial least squares SVR inversion approach," *IEEE Trans. Geosci. Remote Sens.*, vol. 54, no. 11, pp. 6818-6832, Nov. 2016.

[14] L. Poli, G. Oliveri, and A. Massa, "Imaging sparse metallic cylinders through a local shape function bayesian compressing sensing approach," *J. Opt. Soc. Am. A*, vol. 30, no. 6, pp. 1261-1272, Jun. 2013.